Hindawi
International Journal of Antennas and Propagation
Volume 2021, Article ID 5514972, 19 pages
https://doi.org/10.1155/2021/5514972

Review Article

A Review of Synthesis Techniques for Phased Antenna Arrays in Wireless Communications and Remote Sensing

Stanislav Ogurtsov,[1] **Diego Caratelli**,[1,2] **and Zhe Song**[1,2]

[1]*Department of Research and Development, The Antenna Company, 5656 AE, Eindhoven, Netherlands*
[2]*Department of Electrical Engineering, Eindhoven University of Technology, 5600 MB, Eindhoven, Netherlands*

Correspondence should be addressed to Diego Caratelli; d.caratelli@tue.nl

Received 15 January 2021; Accepted 1 September 2021; Published 27 September 2021

Academic Editor: Luciano Mescia

Electronically controlled antenna arrays, such as reconfigurable and phased antenna arrays, are essential elements of high-frequency 5G communication hardware. These antenna arrays are aimed at delivering specified communication scenarios and channel characteristics in the mm-wave parts of the 5G spectrum. At the same time, several challenges are associated with the development of such antenna structures, and these challenges mainly originate from their intended mass production, contemporary manufacturing technologies, integration with active RF chains, compact size, dense circuitry, and limitations in postmanufacturing tuning. Consequently, 5G antenna array designers are presented with contradictory design requirements and constraints. Furthermore, these designers need to handle large numbers of designable parameters of the antenna array models, which can be computationally expensive, especially for repetitive and adaptive simulations that are required in design optimization and tuning. Antenna array synthesis, namely, the process of finding positions, orientation, and excitation of the array radiators, is a challenging yet crucial part of antenna array development. This process ensures that the performance requirements of the antenna array are met. Therefore, there is a need for reliable yet fast automated computer-aided design (CAD) and synthesis tools that can support the development of 5G antenna array solutions, from the initial prototyping stage to the final manufacturing tolerance analysis. This paper presents an overview of recent advances in antenna array synthesis from the viewpoint of their applicability to the design of electronically reconfigurable and phased antenna arrays for wireless communications and remote sensing.

1. Introduction

Phased antenna arrays play a pivotal role in the development of upcoming 5G communication systems. Owing to spatial filtering and real-time pattern adaption capabilities, antenna arrays exhibit excellent wireless channel characteristics that are instrumental in achieving high data rates and reliable quality of service, especially in the millimeter-wave frequency range of the 5G spectrum [1–5]. For decades, the phased arrays have been developed as rather bulky, expensive, stationary, or onboard antenna systems for radars, satellite, and cellular wireless communications [6–8].

Recent advances in electromagnetic (EM) computer-aided design (CAD) software [9–12], antenna manufacturing technologies [13–15], solid-state electronics in silicon-based technologies [16–19], millimeter-wave test instrumentation, and computational tools such as graphics processing units, allow for the development and industrialization of compact and cost-effective active phased antenna arrays with integrated electronically controllable beamformers. These products are suitable for 5G applications that are not just associated with base stations of network cells but also with extenders, repeaters, access points, and mobile terminals [1–3]. Each application requires a tailored antenna array performance.

Thus, antenna designers need reliable and versatile array design procedures that can address challenging problems relevant to the synthesis of radiation patterns based on different masks, while handling multiple antenna performance parameters simultaneously, with a reasonable

demand in terms of computational resources and time. Robust techniques should be able to perform syntheses with array models for different levels of complexity, ranging from distributions of isotropic uncoupled radiators to rigorous electromagnetically characterized models of array apertures where antenna mutual coupling effects are properly addressed [20, 21]. The use of a specific antenna array synthesis technique can be maximized by implementing a user-friendly interface and enabling software integration with commonly used electromagnetic computer-aided design (CAD) tools [9–12].

The antenna array synthesis is an automated process of identification or optimization of a specific antenna array model, namely, a procedure for determining the dimensional parameters and the (amplitude and/or phase) excitation tapers across the array aperture and terminals that are useful to meet given performance requirements. This ensures that the performance requirements, associated with the radiation pattern masks, are met in a certain antenna operational state. These requirements are usually essential in instances such as those occurring when pointing the main lobe along a certain direction in transmit (Tx) mode or while enforcing pattern nulls in specific angular sectors in the receive (Rx) mode.

The antenna characteristics considered in the framework of an array synthesis procedure include but are not limited to

Radiation pattern properties over spatial directions, such as the main lobe half-power beamwidth (HPBW), null-to-null beamwidth, sidelobe level (SLL), grating lobe intensity, and front-to-back ratio (FBR)

Power-related figures of merit such as peak directivity, gain, total efficiency, effective aperture, and antenna temperature

Circuital characteristics at the array terminals, such as scattering parameters (input reflection and coupling coefficients) and active (apparent) impedance

Depending on the selected synthesis method or its particular realization, one or a few antenna parameters affect the array design goal function. Other characteristics can be controlled by incorporating specific constraints in the problem formulation. While certain antenna array features, primarily main lobe shape and sidelobe levels, can be evaluated using simple analytical techniques, total efficiency and scattering parameters can only be evaluated using full-wave electromagnetic modeling.

The development, realization, and applications of antenna array synthesis is an expanding research area, and several novel studies have emerged in the technical literature and new dedicated CAD tools have been introduced in the market. Therefore, providing an up-to-date detailed overview of this subject could be a rather ambitious task. Nevertheless, in this study, we have attempted to review the performance of phased antenna arrays in 5G applications through the perspective of an engineer.

2. Iterative Synthesis Methods

2.1. Iterative Fourier Transform Method for Array Pattern Synthesis. Most of contemporary approaches for the numerical synthesis of antenna array patterns are based on the dimensioning of the radiating aperture and evaluation of the excitation tapers through suitable optimization processes. Said approaches are aimed at the minimization of a given objective function that encodes the design specifications and targeted radiation pattern masks. The major differences between optimization procedures can be highlighted through various factors such as the objective function, modeling fidelity, selection of numerical minimization algorithm, and incorporation of design constraints. Both gradient-based and population-based (metaheuristic) optimizers have their own advantages and limitations. Optimizers developed as population-based algorithms are widely used to overcome problems in antenna array synthesis. A different approach for array pattern synthesis is referred to as the iterative Fourier transform (IFT) or iterative fast Fourier transform (IFFT) method. Such technique is rooted in the fundamental relations between antenna array quantities.

The benefits of the IFT method for phased array synthesis were first highlighted in Ref. [22], to the best of our knowledge, as an application of the error reduction algorithm [23]. In Ref. [22], a block diagram of the IFT was presented as it applies to antenna array synthesis. In addition, in Ref. [22], a detailed matrix-vector formulation of the IFT was listed, and it presented criteria for algorithm convergence, which was numerically studied and demonstrated through a power pattern synthesis. This study considered an eight-element linear array with the main lobe directed toward a desired signal and targeted pattern nulling in six discrete directions of jammers of different intensities. In Ref. [22], the potential benefits of the IFT based on two-dimensional discrete Fourier transforms for the synthesis of arbitrarily shaped planar array apertures were discussed.

An illustration of the application of the IFT method to design a synthetic aperture radar (SAR) antenna was given through transmit (Tx) and receive (Rx) pattern syntheses subject to masks concerning the main beam gain ripple, gain slope, and SLLs [24]. Taper syntheses in the short dimension of the SAR antenna were conducted for 48 elements with a separation of 0.7λ, with λ denoting the free-space wavelength. The Tx and Rx patterns were subsequently synthesized with different degrees of freedom (phases for the Tx pattern, amplitudes, and phases with five-bit control for the Rx pattern) to finally generate a two-way pattern of the prescribed characteristics [24].

The similarities between the IFT method and those used for the phase-less synthesis of reflector antennas as well as alternation/successive projection methods have been reported in Ref. [24]. The four essential steps of the IFT method were outlined in Ref. [24], unfortunately without a proper description of the implementation details, in particular, those related to pattern adaptation. The IFT method was further developed to solve synthesis problems of large phased planar arrays [25]. In fact, the IFT (IFFT) method

was specifically developed to handle typical sizes, aperture shapes, requirements, operation modes, and underlying EM interactions of large naval and military phased arrays.

The IFT method is based on the fact that the array factor (AF) and excitation taper are related to each other through a truncated series of direct and inverse Fourier transforms, respectively. A direct Fourier transform (FT) performed on the AF simultaneously produces all the entries of the excitation taper. An inverse FT performed on the excitation taper simultaneously produces AF values for sampled direction cosines [25]. These two stages are performed sequentially and iteratively using fast Fourier transforms (FFTs) with the adaptation of the newly computed data sets to the enforced requirements and design constraints (AF pattern masks, amplitude-only or phase-only taper, and on/off-element state) before being used as the input to the following stage. Only the excitation coefficients corresponding to the grid of the array elements are supplied to the inverse FFT at each iteration. A block diagram of the IFT algorithm is presented in Figure 1.

The IFT method is outlined as follows. The AF of a planar antenna with a rectangular aperture can be defined as a truncated double series of a two-dimensional discrete inverse FT [25]:

$$\mathrm{AF}(u,v) = \sum_{m=0}^{M-1}\sum_{n=0}^{N-1} a_{mn} e^{j2\pi\left(ms_x u + ns_y v\right)}, \tag{1}$$

where $u = \sin\theta\cos\phi$, $v = \sin\theta\sin\phi$, s_x and s_y are, respectively, the x- and y-directional uniform element spacings normalized to the free-space wavelength λ, a_{mn} is the excitation taper entries, and M and N are the number of elements in the x- and y-directions, respectively. The AF is a periodic function of the direction cosines with the u- and v-periods determined by the array element spacings as $-0.5/s_x < u < 0.5/s_x$ and $-0.5/s_y < v < 0.5/s_y$, respectively. Thus, relevant information about the AF can be retrieved by sampling over the rectangle of the direction cosines. For element spacings smaller than a half-wavelength, the AF extends to the invisible space of the direction cosines. At the same time, a part of the (u, v)- direction resides out of the visible space. Therefore, the AF extension into the invisible space must be included in the calculation of the excitation taper entries using direct FFT to avoid degradation of sidelobe characteristics in the process of beam scanning and/or raising of the operating frequency [25].

The IFT method is successfully applied to the synthesis of low-SLL patterns. The first step is the calculation of the AF along the K^2 far-field directions using an initial excitation taper for a given array aperture with $M \times N$ elements. Any excitation taper that causes a reasonably shaped main lobe can be used as the initial one. Subsequently, the pattern of the calculated AF is compared with that of the pattern mask. The AF pattern values above the sidelobe mask are reduced in amplitude to match the mask levels. The AF values below the mask levels and those corresponding to the main lobe remain unaltered. Subsequently, the AF dataset corrected in this way is provided as the input to the direct FFT, which yields the updated excitation taper for the next iteration. The

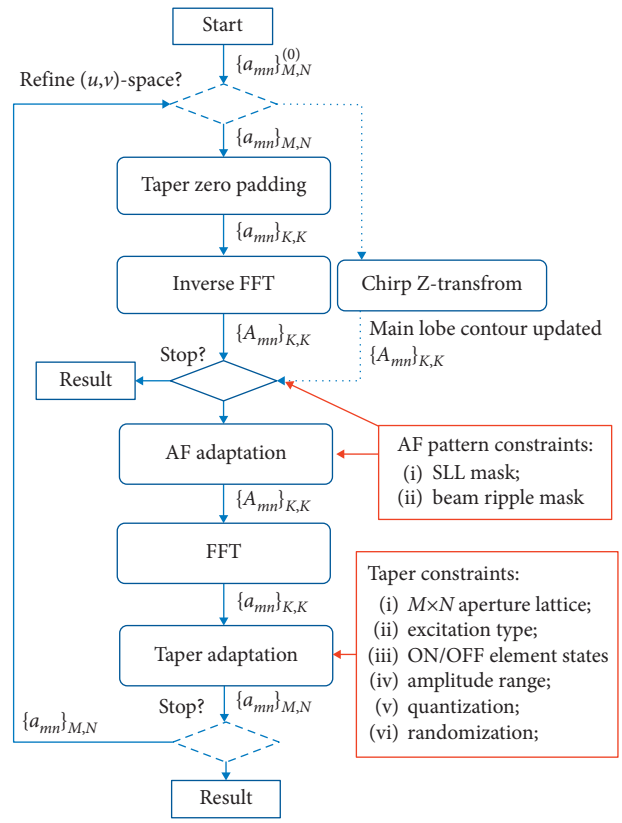

Figure 1: Diagram of the error reduction algorithm [22–24] and IFT method [25–35] as applied to planar phased antenna array synthesis.

updated excitation taper has K^2 entries, although only $M \times N$ of those actually populate the array aperture. The excessive entries should be removed, and iterations should be continued if a complex-valued taper is allowed. If the required pattern characteristics are to be achieved by means of an amplitude-only or phase-only synthesis, the excess information (e.g., computed phase values in the amplitude-only synthesis or nonuniform amplitudes in the phase-only synthesis) is restored to the initial values before proceeding to the next iteration.

Because the main lobe contour, which is corresponding to the first nulls, typically widens as the sidelobes decrease from iteration to iteration, there might be a need to recalculate the main lobe contour repeatedly and with high accuracy, that is, with a refined sampling of the (u, v)-space. A two-dimensional chirp Z-transform can serve as an effective solution to overcome the aforementioned problems [25]. The violations of the sidelobe mask and/or the power content of the excitation taper outside the array aperture are typically used for convergence monitoring and/or termination criteria.

The IFT method is also applicable to triangular array lattices upon affine transformation mapping the original grid onto a suitable Cartesian one [26, 36]. The effectiveness and robustness of the IFT method, along with its ability to synthesize, at very modest computational costs, ultra-low sidelobe sum, and difference patterns for array apertures of

various shapes and comprising a very large number of elements have been demonstrated in various examples [25, 26]. A few examples of the amplitude-only synthesis of ultra-low sidelobe (better than −71 dB) sum and difference patterns for circular and elliptical array apertures with triangular lattices comprising 5797 and 5509 elements, respectively, have been reported in Ref. [25]. Examples of the achieved pseudocontour patterns are shown in Figure 2.

Here, the computational burden and quality of the results for array apertures of different sizes have been studied for different sidelobe requirements, including additional ring-level sidelobe masks with amplitude-only synthesized tapers and nulling sectors with complex excitation tapers. It has been reported that patterns with SLLs smaller than −81 dB were synthesized in 20 minutes and patterns with sidelobes below −61 dB were obtained in just a few minutes. The synthesis was carried out on a PC with an Intel Pentium 4 processor with 1 MB L2 cache operating at 2.8 GHz and equipped with 512 MB RAM.

The IFT method can effectively alleviate the gain and SLL degradation in ultra-low sidelobe sum and difference patterns caused by array element failures (up to 30% of array elements). This has been demonstrated through numerical examples of a circular X-band 5800-element array where failed elements were randomly selected across the aperture [27]. It is worth noting that such compensation synthesis can be carried out on conventional laptop computers in relatively short computational times [27].

Another useful application of the IFT method is the synthesis of thinned linear arrays featuring minimal SLLs [28]. Thinning synthesis was performed by setting the amplitudes of the elements with the highest intensity to those with respect to the predefined filling factor (FL) and by setting the amplitudes of other elements to zero during each iteration between the two FFT stages [28]. The fast computational speed (owing to the use of forward and backward FFT) enabled a large number of trials starting with random initializations, for example, 10000 [28], to find the global optimum in terms of SLLs for a given aperture size and FL. The method has been successfully applied to planar half-wavelength-spaced circular apertures with extensions from 25 to 100 wavelengths and subject to 30 and 40% FLs [29], as illustrated in Figure 3. The IFT method shows similar and even lower SLLs, as shown in Table 1 [29], as compared to the statistical density taper approach [37], while the former technique yielded results in a few minutes per case and with 50 trials for each case.

In a recent study, thinning with amplitude tapering syntheses were performed for large circular array apertures (up to approximately 133 wavelengths), which were capable of sum (with 10 dB dynamic range for the synthesized amplitudes) and difference (with 15 dB dynamic range for the synthesized amplitudes) low-sidelobe patterns with and without the addition of nulling sectors [30], as depicted in Figure 4. It should be noted that the difference pattern syntheses of thinned planar array apertures were reported in scientific literature for the first time in Ref. [30].

A significant benefit of the IFT method for array synthesis problems is the ease of implementation owing to the adoption of well-established computational routines and programming environments [31]. Furthermore, the IFT method is at the core of the commercially available specialized environment for the design and analysis of phased array antennas, APAS [38].

A hybrid IFT and taper density technique [39], termed the IFT density taper (IFTDT) technique, is used for thinning of square and circular arrays [40]. In the IFTDT, the IFT method is used to identify the optimal locations of the active (ON) array elements within every aperture ring while minimizing the SLLs [40].

To prevent degradation of the synthesized array pattern in the process of beam scanning not only at the frequency of synthesis but also at higher frequencies, the SLL requirements have to be enforced upon visible and invisible spaces. The synthesis of scan- and frequency-invariant linear and planar arrays featuring ultra-low SLLs using the IFT method has been explained in Ref. [32]. A useful formula based on the FT shift and scale properties, which is applicable to aperiodic lattice arrays, has been presented in ref. [32]. This formula defines the (u, v)-region to perform a scan and frequency robust syntheses:

$$u^2 + v^2 \leq (1 + \sin\theta_m)^2 \left(\frac{f_h}{f_0}\right)^2, \tag{2}$$

where θ_m is the targeted maximum scan angle, f_h is the highest operating frequency, and f_0 is the synthesis frequency. Formula (2) extends the region of the direction cosines to perform the taper synthesis by including the part of invisible space which enters visible space when the main beam is scanned to the maximum scan angle and/or the frequency is increased to the highest operation frequency [32].

A randomization of quantization errors was included in the IFT iterations that performed linear array amplitude-only and phase-only syntheses. This approach was capable of alleviating SLL degradation due to the amplitude and phase quantization introduced by discrete control components of beamforming chains [33].

The IFT method does not account for the mutual coupling effects between antennas [25–33, 38, 39]. On the other hand, it has been concluded that, in planar arrays with 2000 and more elements, mutual coupling corrupts SLLs and other pattern characteristics only to a limited, acceptable, and often negligible extent [34, 35]. Therefore, IFT syntheses are reliable when applied to large apertures (>2000 elements). At the same time, the impact of coupling becomes more apparent as the number of array elements decreases. In particular, it has been observed on the IFT synthesis results that SLLs lower than −45 dB cannot be realized for arrays comprising less than 500 elements if mutual coupling effects are neglected [34].

2.2. Iterative Matrix Inversion Approach for Array Factor Pattern Synthesis. Another iterative approach for linear array pattern synthesis was proposed in Ref. [41]. This approach is similar to the IFT method with respect to the

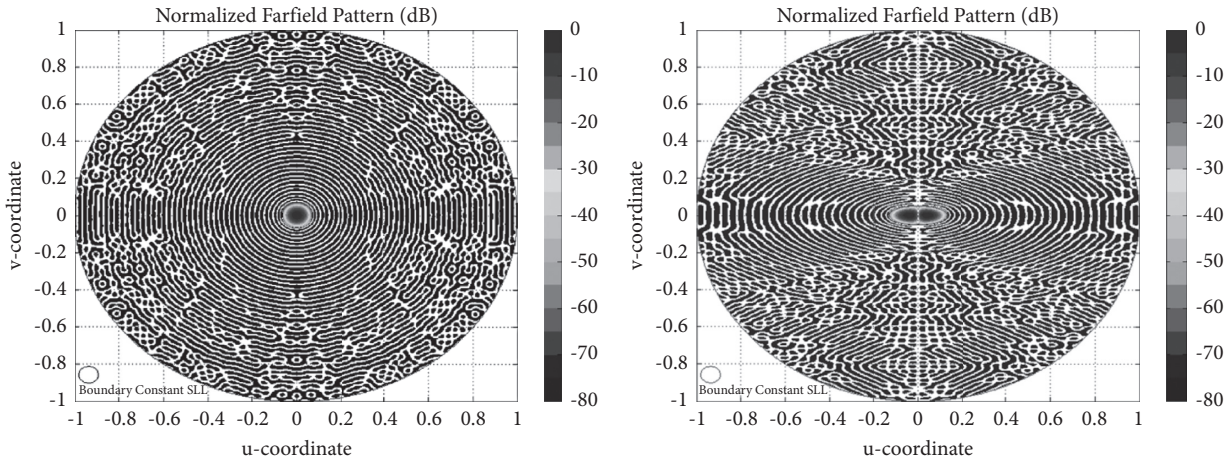

FIGURE 2: Pseudocontour plots [25]: (a) sum pattern of a 1.3 m circular array with 5797 elements operating at 10 GHz; (b) azimuth difference pattern of a 1.9 m × 1.3 m elliptical aperture with 5509 elements operating at 10 GHz. Both patterns, obtained through amplitude-only IFT synthesis, feature a SLL of −71 dB. The array elements are arranged in a triangular grid.

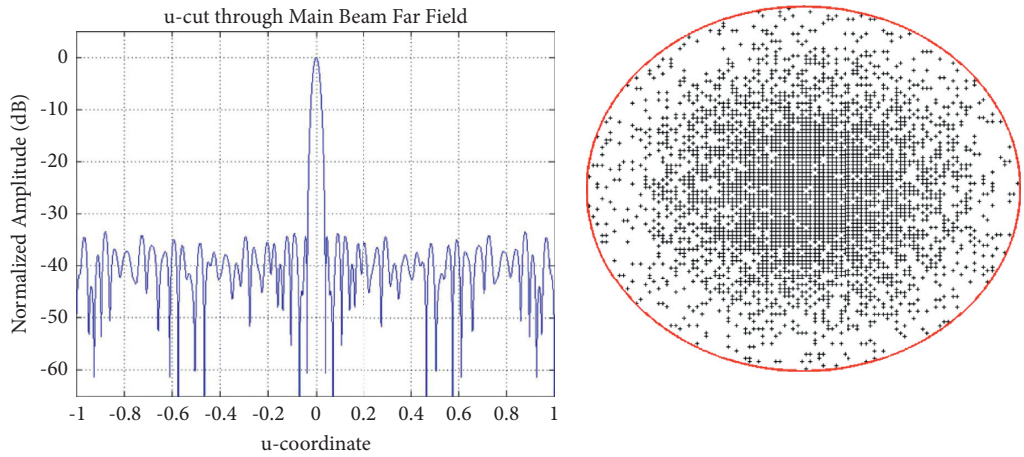

FIGURE 3: A thinned circular aperture array having a diameter of 50λ and based on a 0.5λ spaced square grid with 40% FL. The IFT synthesis results [29]: (a) pattern cut; (b) array architecture with 3116 ON-elements across the aperture.

following factors: (i) iterative computation of the AF pattern from the currently available excitation coefficients, (ii) adapting the computed AF to the required sidelobe mask leaving the far-field samples of the main lobe intact, and (iii) computing the updated excitation taper from the adapted (corrected) AF. A flow diagram of this approach is presented in Figure 5. Contrary to the IFT technique, the approach in Ref. [41] uses information regarding sidelobe peaks, including their angular locations and alternating signs.

The angular locations of the sidelobe peaks are determined and updated iteratively, and then used for computing the excitation taper by solving a suitable system of linear algebraic equations. Such linear system can be solved by means of matrix inversion as described in Ref. [41]. This procedure has been applied to the synthesis of sum patterns of equally spaced centrosymmetric linear arrays comprising up to 38 elements; only a few iterations were needed to achieve the targeted SLLs. As shown in Ref. [41], the number of pattern maxima should match the number of elements in the array. In general, such matching requires numerical experiments to adjust the spacing and/or the number of elements. The same approach has been demonstrated for the synthesis of equally rippled sidelobe patterns relevant to nonuniformly spaced scanning linear arrays; a representative example with 15 elements spanning seven wavelengths is reported in Ref. [42].

The approach in Refs. [41, 42], wherein the iterative procedure is performed through the inversion of a square system matrix, can serve as an effective solution for the synthesis problem, as highlighted in Ref. [43]. In the latter, however, pattern syntheses with complex-valued far-field samples and with far-field samples specified only in magnitude were considered as least square sense solutions for over-determined systems, i.e., when the number of far-field samples is larger than the number of array elements. In

Table 1: The IFT synthesis method: applications and selected features.

Array aperture	Pattern	Elements/ size	Synthesis	Variables	Work
Linear	Sum	8	1 desired direction + 6 discrete deep nulls	NA	[22]
Linear	Shaped Tx Shaped Rx	48	Main lobe shape, sector SLLs ≤ −33 dB, −50 dB	Phases in Tx, phases and amplitudes in Rx, 5-bit control for both	[23]
Circularly shaped with triangular lattice	Sum	5797	≤−71 dB SLL, Chebyshev sidelobes	Unconstrained amplitudes	[25]
Circularly shaped with triangular lattice	Sum	5797	Five level SLLs, −40 dB to −80 dB	Unconstrained amplitudes	[25]
Circularly shaped with square lattice	Sum	3413	Three level SLLs with four rectangular nulling sectors	Unconstrained amplitudes	[25]
Elliptically shaped with triangular lattice	Azimuth difference	5509	≤−71 dB SLL, mostly Chebyshev sidelobes	Unconstrained amplitudes	[25]
Circularly shaped with triangular lattice	Sum, Azimuth difference	5800	−51 dB SLL sum pattern, −48 dB SLL difference pattern, pattern recovery with 5, 10, and 30% failed elements	Constrained amplitudes, 8-bit quantization	[27]
Linear, thinned symmetrically and asymmetrically	Sum	200	SLL minimization with different fill factors (FL), e.g., −24.8 dB SLL achieved with 10,000 trials for 77% FL	On/off element states	[28]
Thinned circularly shaped 0.5-λ-spaced	Sum	7788, 9386	SLL minimization with 30% and 40% FL	On/off element states	[29]
Thinned circularly shaped 0.5-λ-spaced	Sum	25, 50, 100, and 133.3 λ	SLL minimization over the entire (u, v)-cell	10 dB range continuous amplitudes for ON elements, 15 dB amplitudes with nulling	[30]
Thinned circularly shaped 0.5-λ-spaced	Azimuth difference	25, 50, 100, and 133.3 λ	SLL minimization over the entire (u, v)-cell	20B range continuous amplitudes for ON elements	[30]
Linear	Sum	31, 61, 100, 200	SLL minimization with phase randomization	Phases with 3-to-8 bit resolutions	[33]
Linear	Sum, difference	40, 120	SLL minimization with amplitude randomization	20 dB amplitude range with, 4,5,6-bit resolutions	[33]

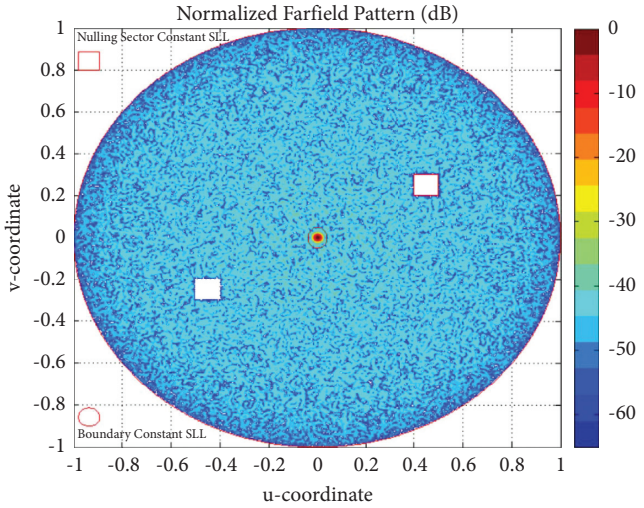

Figure 4: Sum pattern [30] of a thinned 100λ circular array with 0.5λ spaced square lattice and 30% FL as synthesized through the IFT technique with an amplitude-only taper. The pattern features a SLL of −40 dB and two 65 dB depth nulling sectors.

numerical examples of both synthesis cases in Ref. [43], the far-field samples were defined only over the angular quadrant that covered the main lobe.

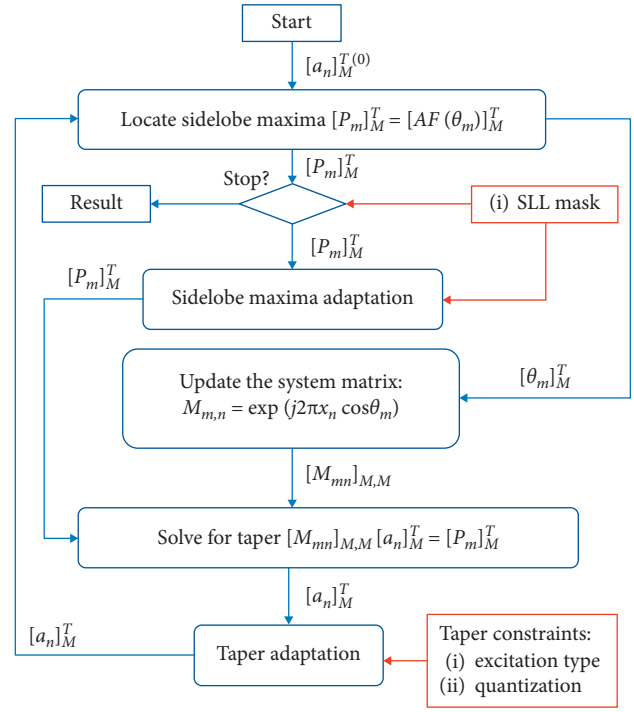

Figure 5: Block diagram of the linear array pattern synthesis technique detailed in Refs. [41, 42].

It is worth noting that the described iterative methods are based on the AF and are not suitable for antenna array syntheses that are associated with additional radiation pattern requirements, such as those relevant to maximal directivity and polarization characteristics. Furthermore, these methods do not account for the nonidentical far-fields of array-embedded elements.

2.3. Array Pattern Synthesis Using Gradient-Based Optimization. The use of population-based algorithms such as genetic algorithms (GAs) and particle swarm optimizers (PSOs) for antenna array synthesis is usually justified by the presence of multiple local optima of the objective function (which, in turn, is related to the AF) over the design space. In such scenarios, gradient-based algorithms are typically considered to be useful for optimization in the vicinity of nominal design. At the same time, numerical examples have demonstrated that array pattern synthesis, when formulated as an optimization problem, does not benefit from the use of population-based algorithms in handling AF-based objective functions. As opposed to contemporary practices, it has been found that array pattern synthesis through gradient-based optimization, combined with a smart random search, provides similar results as compared to population-based techniques, while offering a definitive advantage from a computational standpoint [44–46].

To improve the computational effectiveness of gradient-based optimization and avoid trapping in local minima, it is advisable to (i) utilize analytical derivatives of the objective function, wherever available and (ii) to introduce a reasonable degree of randomness in the solution process.

Analytical expressions can be easily derived for the AF pattern and directivity functions, by using equation (2.30) in [44] for linear array directivity. The smart random search [45] linearly combines a randomly generated point x_{rand} with the current best design x_{best} such that the search procedure is biased towards the global best design as the iteration count i gets closer to the maximum number of iterations $i_{\max}$ allowed for the random search stage [44]:

$$\mathbf{x}^{(i+1)} = \lambda^{(i)}\mathbf{x}_{\text{rand}} + \left(1 - \lambda^{(i)}\right)\mathbf{x}_{\text{best}}, \tag{3}$$

where the scalar $\lambda^{(i)}$ is forced to decay with the iterations, for example, $\lambda^{(i)} = 1 - i/i_{\max}$. Formula (3) was established empirically. Its numerical efficiency for array syntheses has been validated through the heuristic approach described below.

Numerical studies have been conducted on different end-fire linear arrays with $N = 10$, 20, and 40 radiating elements using the corresponding Hansen–Woodyard (H-W) designs as the initial solution proxies [47]. The standard sequential quadratic programming (SQP) algorithm, implemented in the MATLAB *fminimax* routine, was the main optimization engine [48]. For each case, the array synthesis was completed after only a few hundred objective function evaluations, instead of thousand iterations, which is typically required by population-based methods such as GAs or PSOs. The design cases presented in Refs. [44, 45] were aimed at achieving the following goals:

SLL reduction and AF directivity maximization with uniform interelement separation and progressive phase shift as variables

SLL reduction with variable element-specific progressive phase shifts (i.e., with N-1 variables)

SLL reduction with nonuniform element spacing and element-specific progressive phase shifts (i.e., with 2N-2 variables)

SLL reduction with an additional 20 dB suppression over the first sidelobe sector of the H-W design combined with constrained nonuniform element separation and element-specific progressive phase shifts

It is worth noting that the random search stage was necessary for cases with 20 and 40 element arrays wherein element separations and phase shifts were used as variables. In other cases, a direct gradient optimization was sufficient.

The efficiency of the discussed approach has also been illustrated with two synthesis examples of a boresight linear array, one featuring a sum pattern with additional deep nulling sectors, and another featuring a low-sidelobe symmetrical sector-beam pattern in Refs. [44, 46]. In these examples, the array patterns were synthesized using the same number of array elements, the same number of design variables, and the same pattern masks as in the synthesis examples tackled in ref. [49] using Taguchi's method. It should be noted that in the case of the low-sidelobe sum pattern with additional nulling sectors, the gradient-based search technique combined with analytical derivatives [44, 46] yielded the final result after only 300 cost function evaluations without the need of resorting to a random search. Furthermore, the array pattern synthesized using the gradient-based search, shown in Figure 6(a), significantly outperforms the pattern obtained through Taguchi's method (Figure 3 in [49]) in terms of both peak SLL (PSLL) and nulling sector depth.

For symmetrical sector-beam pattern synthesis, the gradient-based search combined with the analytical derivatives of the cost function yielded an optimal solution with a −28.7 dB PSLL after 1500 cost function calls, as shown in Figure 6(b), while the Taguchi's method produced a pattern featuring a −25 dB PSLL (see Figure 6 in [49]) after 4920 cost function calls. The first 1000 cost function calls (out of 1500) in the gradient-based synthesis of the sector-beam pattern in Refs. [44, 46] were invested on the smart random search stage. The same sector-beam pattern problem was synthesized using a particle swarm optimizer [50], where a solution with characteristics similar to the solution generated using Taguchi's method was obtained after 16000 cost function calls.

The gradient-based optimization was used along with analytical derivatives and smart random search (where necessary), also for array synthesis that included array radiators with different far-field and S-parameter characteristics. In such situations (usually when the number of array elements is smaller than 500), full-wave EM simulation tools should not only be used for verification of the final results but also for the main steps in the design process. At the same

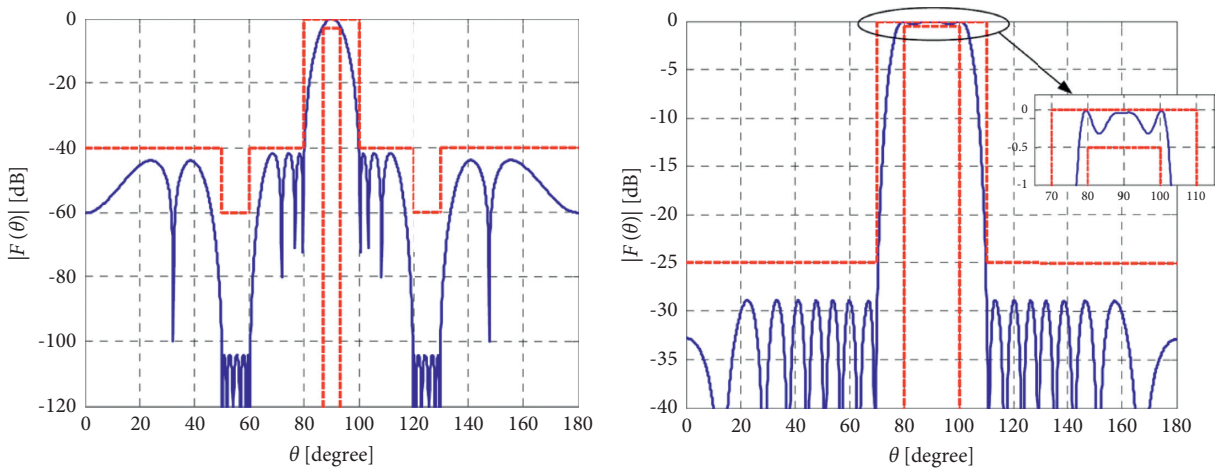

Figure 6: Examples of AF patterns synthesized using a gradient-based optimizer enhanced with analytical derivatives and smart random search [44, 46]: (a) sum pattern; (b) sector-beam pattern.

time, a gradient-based optimizer can efficiently be used to adjust AF-based models during the prototyping stage [44, 51, 52], e.g., as depicted in the flowchart of Figure 10.17 in Ref. [44] or Figure 4 in Ref. [51]. In addition, gradient-based search methods have been used in the simulation-based design of low-sidelobe arrays for the following tasks [53]:

To find the corporate feed architecture and constrained power-split ratios of the feed junctions (see Step 2 in Figure 7)

To optimize the EM-based response-surface model (smooth kriging surrogate) of array feed junctions, using the Matlab *fmincon* routine [48] (see Step 5 in Figure 7)

To fix the SLL degradation due to coupling and interactions within the feed connected to the array aperture (see Step 9 in Figure 7)

It is worth noting that the gradient-based routines can not only successfully optimize smooth surrogate models, as depicted in Figure 7, but also optimize the original high-fidelity models (configured from accurately simulated far-fields [54]), e.g., the models of planar apertures depicted in Figure 8, which require higher computational costs, mostly due to the acquisition of accurate far-field characteristics.

3. Deterministic Array Pattern Syntheses with Nonperiodically Distributed Antenna Elements

3.1. Synthesis Based on the Auxiliary Array Pattern (AAP). The design of sparse antenna arrays is receiving huge attention mainly thanks to meaningful advantages such as a reduced number of antenna elements, reduced weight, and complexity of feeding networks, as well as a larger average interelement separation which alleviates thermal and parasitic EM-coupling effects. In addition, properly synthesized arrays with aperiodic element separations produce no main lobe replicas in the visible space, even while scanning. Nonperiodic architectures can also mitigate cost-related issues for conformal antenna arrays, which offer compelling advantages in terms of electronic beam scanning, visual unobtrusiveness, and noninterference with the aerodynamic characteristics of the host body (e.g., aircraft, satellites, and different categories of terrestrial vehicles). The design of conformal arrays, however, poses additional challenges compared with planar topologies. It should be noted that the adoption of population-based techniques for the synthesis of sparse arrays with nonperiodically distributed radiators in problems with a significant number of unknowns usually results in very large synthesis times. In this context, deterministic methods are preferable.

A method based on the concept of the auxiliary array pattern (AAP) function was developed to analytically determine the optimal element density and excitation tapering distributions to mimic a given radiation pattern [55–57]. Thus, the array sparseness can be conveniently tuned to meet the design requirements in terms of minimum separation between different antenna elements and maximal array aperture size. This approach does not require optimization or iterative procedures to perform the synthesis, thus reducing the design time.

The AAP approach has been elaborated further to handle conformal array apertures [58, 59] subject to different pattern masks and structure constraints, similar to those illustrated in Figures 9–12. It has been proven that this procedure allows for complex synthesis problems, subject to specific requirements associated with pattern magnitude and phase masks, maximum aperture size, minimum interelement spacing, or maximum number of power levels to be operated in the beam-forming network. These requirements need to be addressed in a straightforward and computationally inexpensive manner [59].

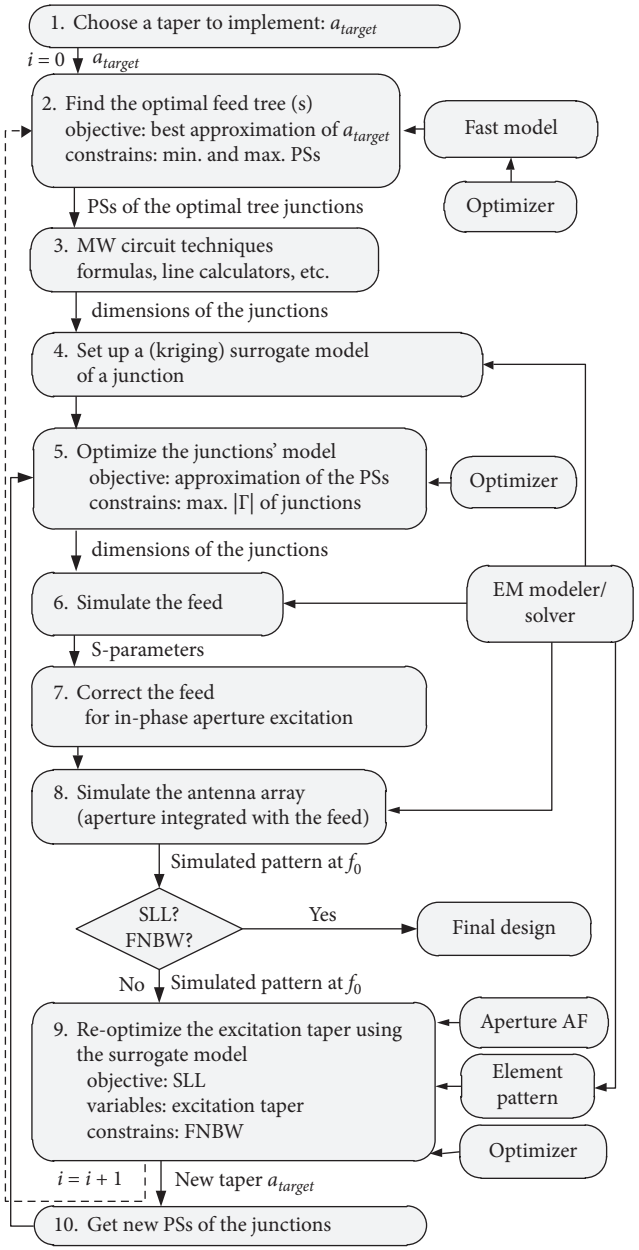

Figure 7: Process diagram of a surrogate-assisted design of low-sidelobe linear arrays inclusive of corporate feeding network [53]. PS stands for the feed junction split ratio, $|\Gamma|$ denotes the general reflection coefficient at the junction input, **a** stands for the excitation taper, and f_0 is the working frequency. The AF is used at Steps 2 and 9. A more general realization of the design process can search for and implement a new optimal architecture after Step 9.

3.2. Synthesis Using the Array Dilation Technique (ADT). The Array Dilation Technique (ADT) is another deterministic approach which has been recently proposed in ref. [60]. At a conceptual level of description, the ADT stretches a linear array in analogy to an elastic strip, thus leading to aperiodicity and sparsity in the linear array lattice. As presented, the ADT handles isophoric symmetric linear arrays, namely, centrosymmetric arrays with uniform excitation. Thus, it does not rely on any excitation tapering; instead, it modifies the interelement spacings in a uniformly fed array with an originally uniform lattice. The ADT achieves comparatively lower SLLs for optimal thinning levels [61] as compared to previously published approaches [60]. The ADT is a noniterative method that can be used to determine the nonuniform separations between array elements so as to yield the lowest possible SLL for a particular partitioning and impose constraints on the interelement spacing. The ADI dilates the linear array lattice according to Ref. [58]:

$$d_n = d_0 \left\{ 1 + \frac{\alpha_J}{N_t} (|n| - 1) \right\}, \tag{4}$$

where d_0 is the initial element separation, N_t is the total number of elements in the modified lattice, the index n runs over half of the element separations, and α_J is the dilation parameter in a given partitioning, such that the element separation d_n in that particular lattice part varies from d_0 to $\alpha_J\, d_0$. In Ref. [60], α_J took values from {0, 1, 2, 3, 4}.

The value for the innermost element separation (one separation for the even number of elements and two separations for the odd number) was set to d_0 in the numerical studies. Array lattice geometries corresponding to different combinations of dilation parameter values were enumerated for a given number of array elements and the initial (innermost) separation d_0 (both representing the original lattice). Each lattice geometry was characterized by AF directivity, HPBW, SLL, PSLL, average SLL, first sidelobe intensity, and average element separation. In particular, AF directivity was assessed using analytical expressions [62]. Several case studies have demonstrated that ADT can be used for syntheses of isophoric linear array lattices with minimal possible SLLs. The array geometry with the lowest peak SLL is identified among the enumerated array geometries [60]. The range of the direction cosines (see equation (2)), over which the enumerated array SLLs were evaluated, was not specified in Ref. [60].

The various test cases included the following:

Low-SLL synthesis with 17, 37, and 2000 elements subject to no constraints on the array length and starting from a half-wavelength-spaced lattice

Low-SLL synthesis with 17, 37, and 2000 elements and fixed array lengths starting from a half-wavelength-spaced lattice

Synthesis for grating lobe suppression with 37 elements starting from a wavelength-spaced lattice

A comparison of the ADT-synthesized linear arrays with respect to PSLL and other performance characteristics (where available) was given, and results were obtained using several other methods [60], where the ADT-synthesized arrays demonstrated similar or even better characteristics. Selected ADT-synthesized lattices were implemented and simulated as array apertures comprising cavity-backed microstrip patch antennas; their scan performance has also been demonstrated experimentally. A noticeable feature of ADT-synthesized linear arrays is that, although their

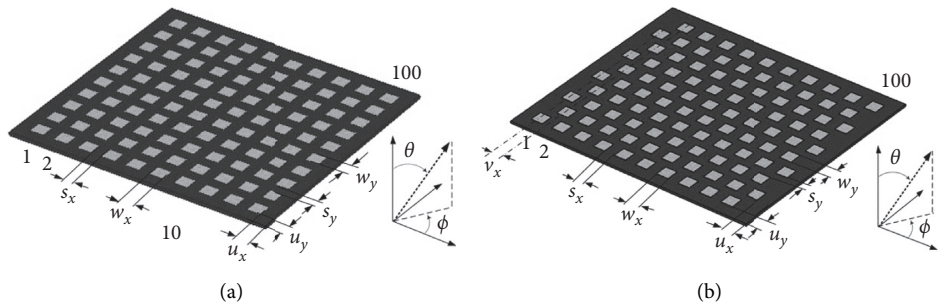

Figure 8: Planar array apertures comprising 100 linearly polarized microstrip patch antennas: (a) Cartesian grid; (b) triangular grid. Phase-only syntheses for reduced SLLs were performed using EM-simulated models in Ref. [54].

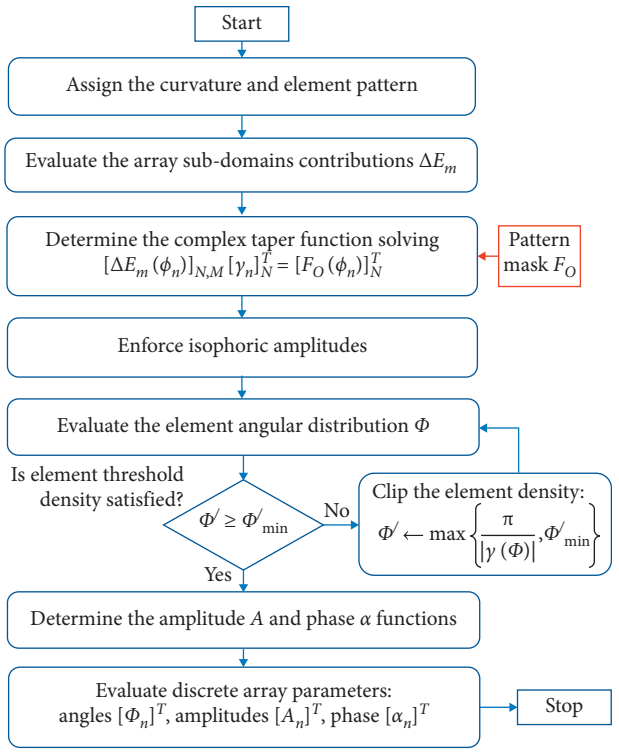

Figure 9: Diagram of the AAP technique for conformal array synthesis with constraints on the structure layout [58].

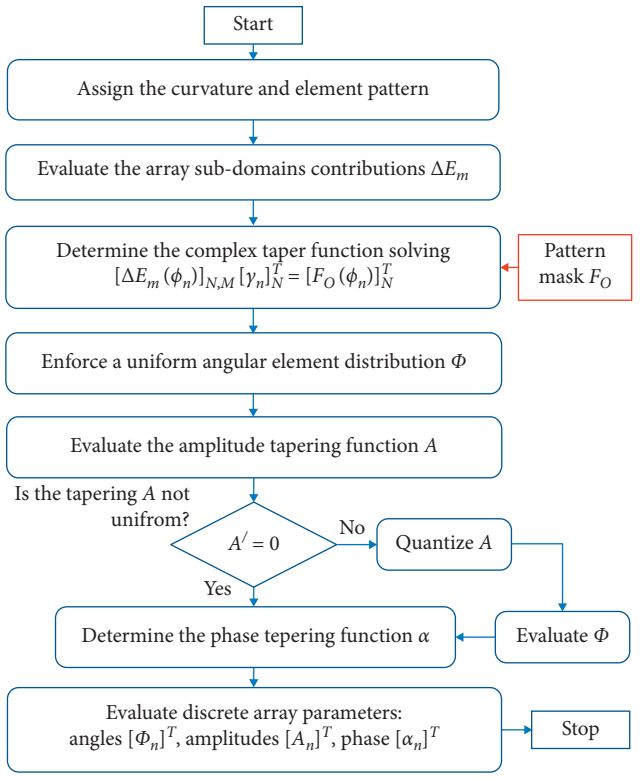

Figure 10: Diagram of the AAP technique for array synthesis with a quantization of the excitation amplitude [58].

scanned AF patterns show a definite degradation of the PSLL, wide angular sectors with low SLL persist next to the main lobe, as illustrated in Figure 13.

4. Phased Array Pattern Synthesis with Nonidentical Array Element Far Fields

It can be inferred from recent scientific publications on the development of phased antenna arrays for 5G applications [63–76] that array pattern synthesis requires the selection or evaluation of the following parameters and characteristics for the initialization of the synthesis procedure: the number of array elements, the aperture size, the separation between array elements (cell size), the array aperture lattice, as well as the detailed design of the individual array element including the relevant stack-up, polarization (single or dual per element), and spatial orientation along the radiating aperture. Such settings are aimed at system-level specifications and account for the adopted (or designed) beamforming integrated circuit (BFIC) solution and the host printed circuit board (PCB) manufacturing technology (including dimensional restrictions defined by the PCB design rules). In the context of array pattern synthesis, the adopted BFIC delivers a certain gain range, amplitude, and phase-control resolutions and errors in Tx and Rx mode. The design of Wilkinson's divider/combiner networks typically stays out of the scope of radiation pattern synthesis in the case of active phased arrays with fully RF beamforming chips.

In a phased-array development process, pattern synthesis serves as an effective means to fill a reliable and operation-mode-specific scan table to meet the required design specifications concerning several factors, such as effective isotropic

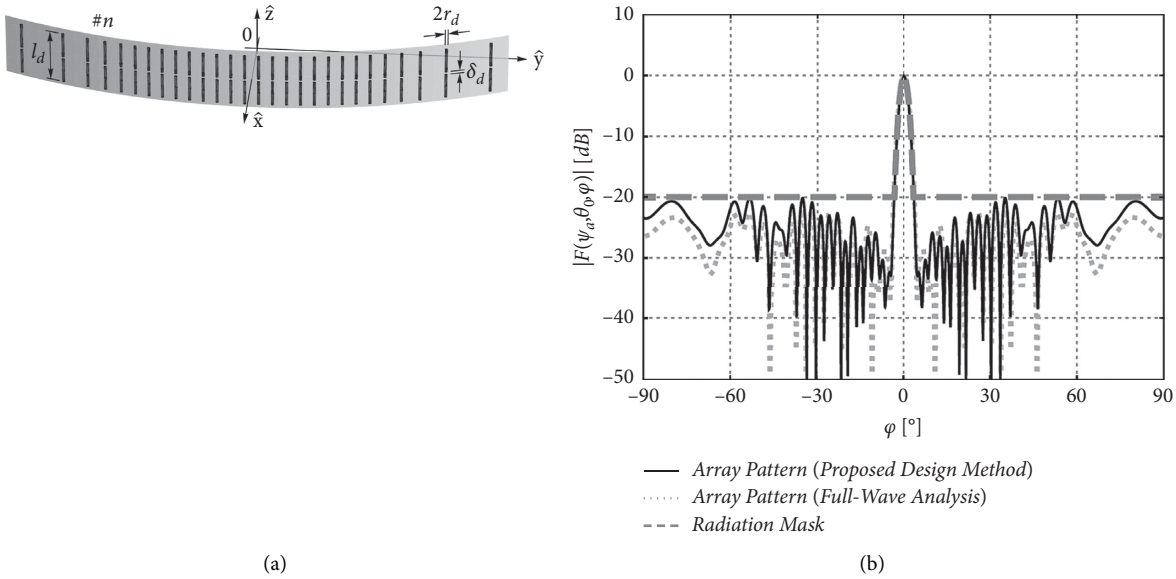

Figure 11: Synthesized sparse 24λ-long arc array aperture with curvature radius of 30λ and 28 antenna elements that features an HPBW of 6 degrees and SLL of −20 dB [59]: (a) physical implementation where each array element is a 0.425λ long dipole antenna with 0.0125λ radius and 0.005λ feeding delta gap; (b) magnitude of the array radiation pattern.

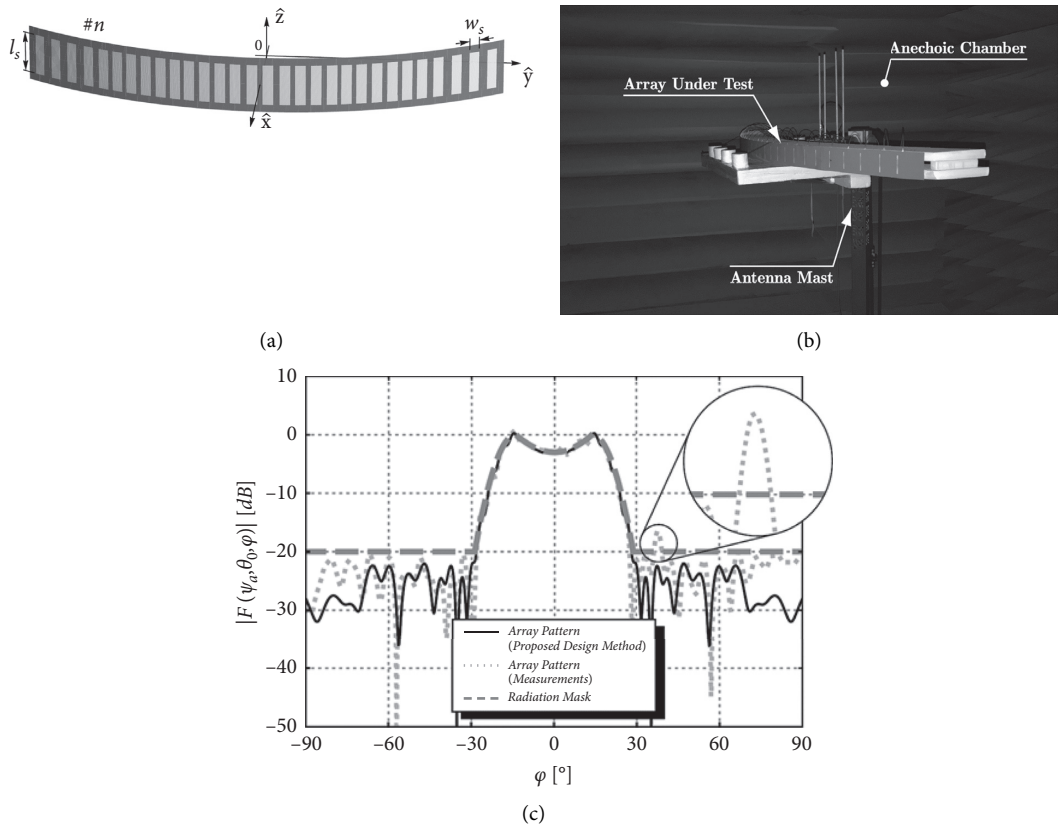

Figure 12: Synthesized sparse 23λ-long arc array aperture with curvature radius of 21λ and 30 antenna elements that features an isoflux radiation pattern [59]: (a) physical implementation based on 0.607$\lambda \times$ 0.0367λ slot antennas; (b) 5 GHz prototype under test; (c) synthesized and measured array radiation patterns.

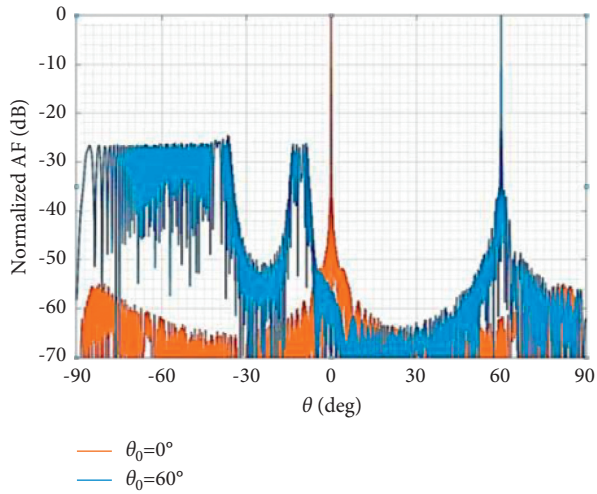

FIGURE 13: Normalized AF patterns featured by an isophoric 2000-element sparse linear array with antenna separation $d_0 = 0.5\lambda$ at the scan angles of 0 and 60 degrees [60]. The array was synthesized with no constraint on the overall length, which, eventually, was extended up to 1344.2λ.

radiated power (EIRP), polarization purity, cross-polarization interference and discrimination, scan range, scan loss, and active reflection coefficients. Note that, wherein the array aperture dimensions are fixed, the excitation tapers appear to be the only essential degrees of freedom in the synthesis procedure. While 5G base stations operating at sub-cm and mm-wave frequencies are likely to require 64 to 256 (or more) radiating elements per array aperture so as to achieve the desired peak EIRP level, 5G customer premise equipment (CPE) operating at sub-cm and mm-wave frequencies is expected to rely on phased arrays with approximately 8 to 32 radiating elements. Thus, the differences in terms of embedded element far-field characteristics can be significant and should be properly accounted for.

In such circumstances, a reusable accurate EM model for phased array synthesis, illustrated in Figures 14 and 15, can be implemented on the basis of the superposition principle, through a complex-valued vectorial summation over all the array aperture inputs:

$$\mathbf{E}(\mathbf{r}) = \sum_n a_n \mathbf{E}_n(\mathbf{r}), \tag{5}$$

where the summation index n runs over the antenna elements in the case of single-polarization radiators and over the antenna input ports in the case of radiators supporting dual, supposedly orthogonal, polarizations.

In (5), $\mathbf{E}$ stands for the total electric field; $\mathbf{E}_n$ stands for the EM-simulated (or measured) electric fields due to the separate excitation of the input port n at the relevant BFIC TX-output/RX-input pin, and a_n is the complex wave exciting the n-th port, namely, the n-th entry of the excitation taper, at the frequency of operation f_0. Note that the field terms $\mathbf{E}_n$ in (4) are evaluated in the same coordinate reference system (a default option of the state-of-the-art EM simulation environments) such that the phase correction associated with the radiator location is directly embedded in $\mathbf{E}_n$. It should also be noted that the radial vector r is defined, for all the $\mathbf{E}_n$, starting from the origin of the adopted coordinate system.

Therefore, the summation in (5) allows quantifying the field-related characteristics at the working frequency f_0 at any point $\mathbf{r}$ in space, including the near-field region. In the far-field region, it is convenient to cast (5) in the following form:

$$\mathbf{E}(\theta, \phi) = \sum_n a_n \mathbf{E}_n(\theta, \phi), \tag{6}$$

where the distance r is regarded as a parameter. In practice, r is set equal to a certain value (i.e., $r = 1$ m) during the post-processing of the EM-simulated data for the evaluation of the general far-field quantity $\mathbf{E}_n$.

Moreover, state-of-the-art simulation environments also allow for the embedded far-field distributions to be computed by referring to an element-specific (local) coordinate system, such that the phase terms associated with the element locations across the aperture can be evaluated as

$$\mathbf{E}(\theta, \phi) = \sum_n a_n \mathbf{E}_n(\theta, \phi) e^{\mathbf{j}\mathbf{k}\cdot\mathbf{R}_n}, \tag{7}$$

where the wave propagation vector $\mathbf{k} = k\ [u, v]^T$ incorporates the direction cosines, $\mathbf{R}_n$ denotes the location of the n-th element along the array aperture, and the complex far-field term $\mathbf{E}'_n$ is computed referring to the location of the n-th element parametrized through the shift vector $\mathbf{R}_n$.

Equation (7) can be simplified into AF with the assumption of identical far fields E_n, by moving the far fields out of the sum. On the other hand, an accurate modeling of the electromagnetic field characteristics of phased arrays is only possible using (5)–(7). Such EM-based modeling is necessary to reliably quantify cross-polarization interference/discrimination, especially for apertures that simultaneously generate beams with orthogonal polarization

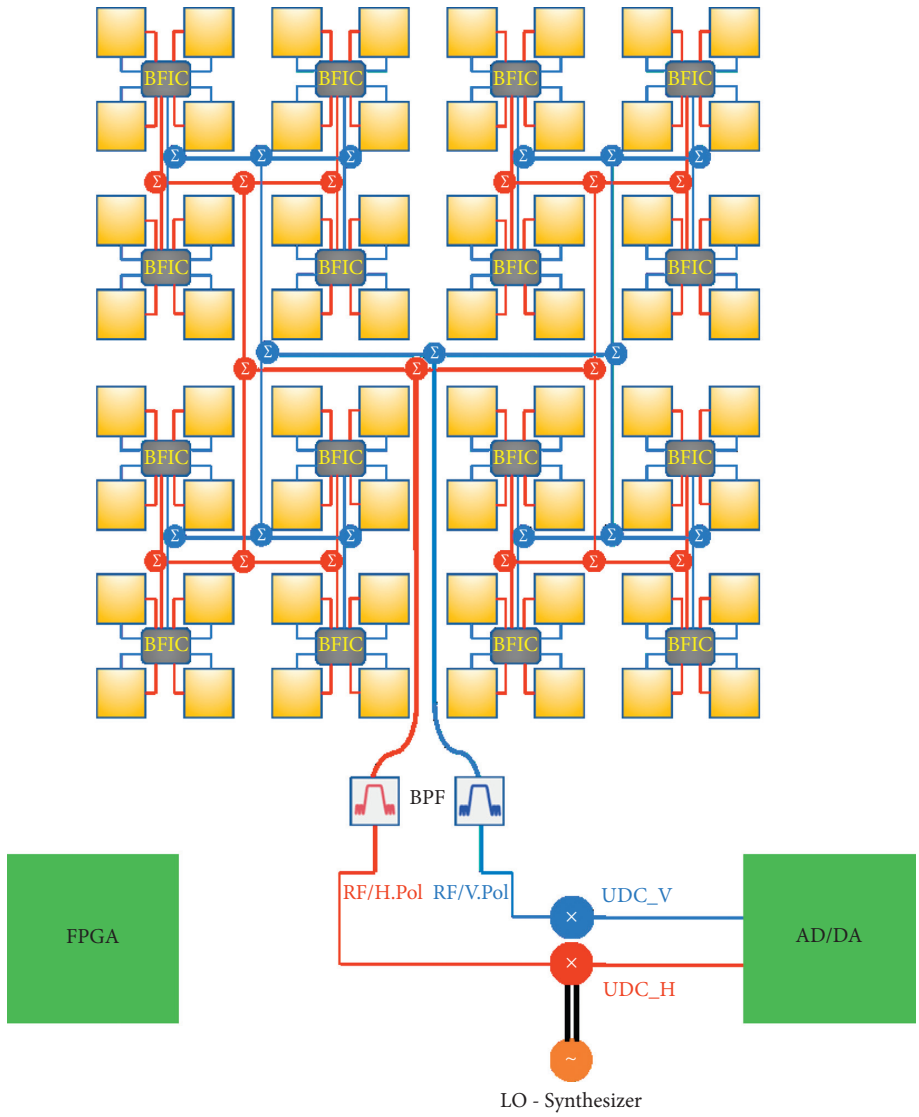

FIGURE 14: Diagram of a 5G phased array antenna capable of dual-beam operation and comprising 64 dual-polarized radiating elements, this resulting in 2×64 array inputs. Every beamforming integrated circuit (BFIC) is connected to 8 antenna inputs/outputs (with each dual-polarized antenna having two inputs/outputs) and has two common inputs/outputs (one per polarization as indicated with the blue and red color lines) connected to polarization-specific Wilkinson's networks.

characteristics. Note that the element-specific amplitude and phase behavior of $\mathbf{E}'_n(\theta, \phi)$ is preserved in (5)–(7) to the full extent, whereas some information is lost in the AF-based modeling. For planar array apertures, (7) can be rewritten as

$$\mathbf{E}(u, v) = \sum_n a_n \mathbf{E}_n(u, v) e^{jk(x_n u + y_n v)}. \quad (8)$$

Although the element far-field terms $\mathbf{E}_n$ are not known over the entire (u, v)-space, their analytical continuation into the invisible space allows using (8) to evaluate the total far-field distribution over the entire space, thereby enabling the analysis of the array scanning performance.

Another important aspect in phased-array pattern synthesis is that the total far-field representation based on (5)–(8) is an accurate reusable model with well-defined analytical derivatives with respect to the excitation taper entries (that constitute the available degrees of freedom for the synthesis problem). The cost associated with the acquisition of such EM model equals the product of the total number of input ports and the simulation time of the array with aperture [51, 52, 54]. Thus, minimax routines enhanced with analytical derivatives similar to those in Ref. [48], and combined with the smart random search, are well suited for phased array synthesis for SLL minimization, pattern nulling, cross-polarization minimization, and polarization interference minimization. Syntheses of planar and linear apertures based on this methodology have been conducted and described in Refs. [54, 77], respectively. A few selective results are shown in Figures 16 and 17. A surrogate-based modeling was used in Refs. [51, 52, 54, 77] so as to reduce the

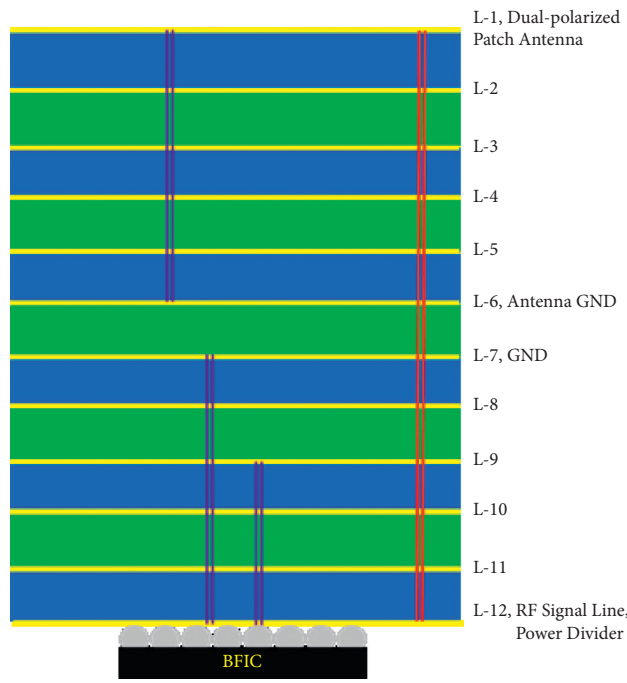

Figure 15: Simplified diagram of a low-cost PCB stack-up for 5G phased antenna arrays.

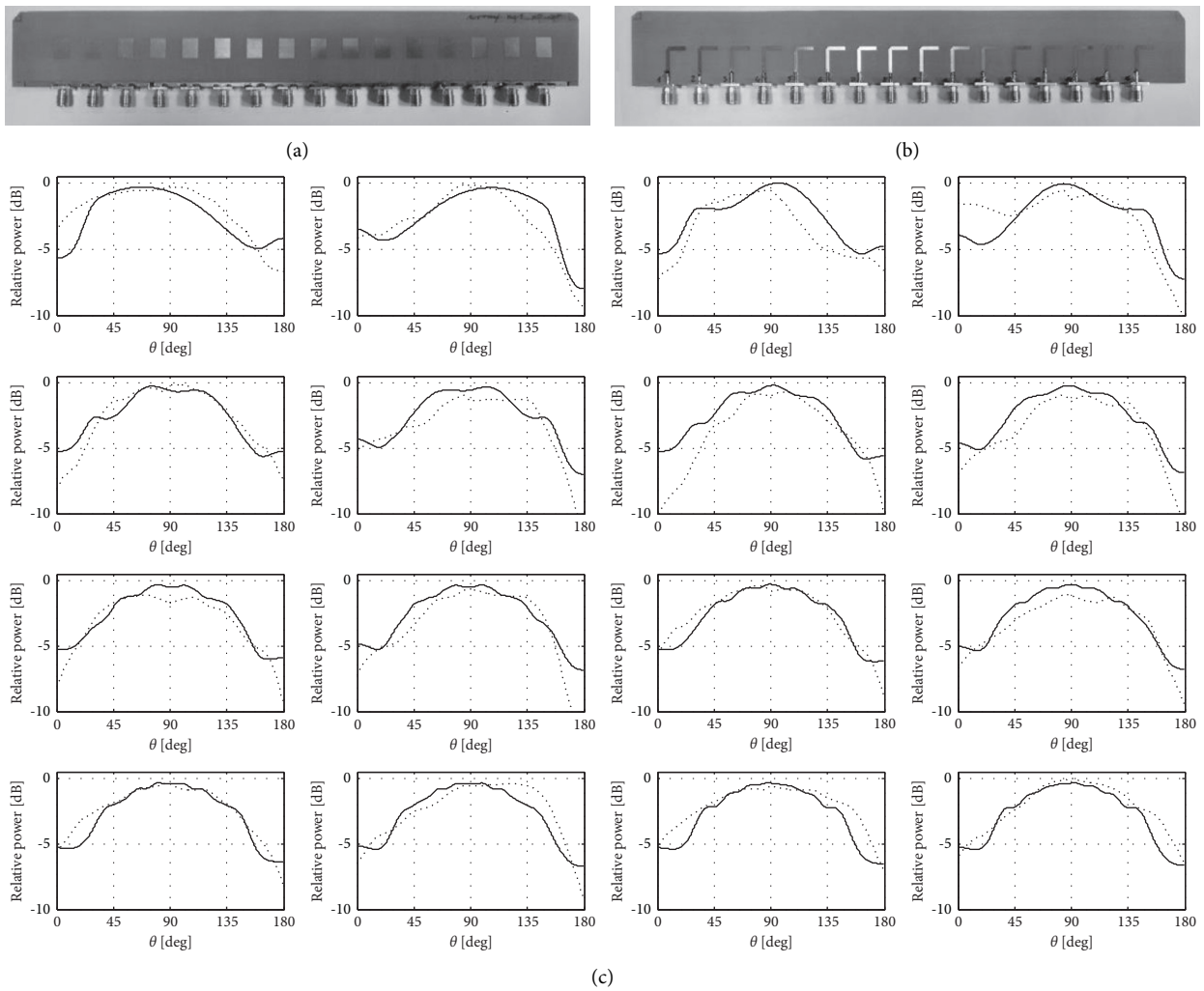

Figure 16: Antenna array operating at 10 GHz [77]: (a) front view; (b) back view; (c) measured (. . .) and simulated (▬) aperture-embedded-element E-plane patterns. The measured and simulated radiation patterns are normalized, respectively, to the maximal measured and simulated values. The patterns are displayed from top to bottom as follows: 1 and 16 (outermost elements), 2 and 15,. . ., 7 and 8 (central elements).

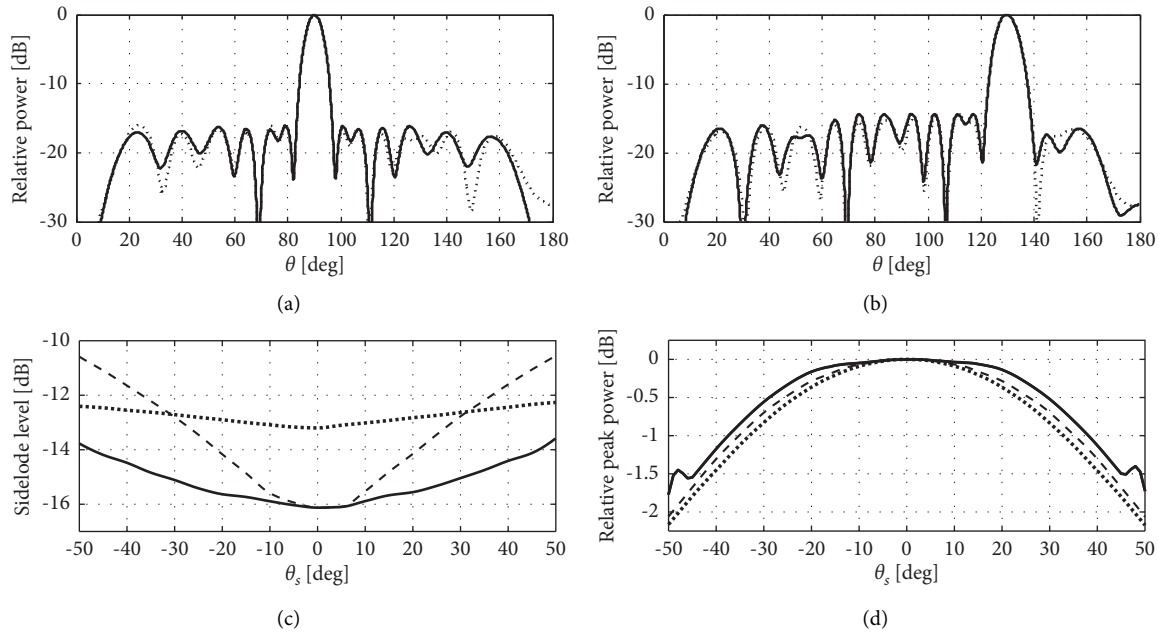

Figure 17: Selected radiation patterns at 10 GHz of the array shown in Figure 16 as obtained by phase-only synthesis [77]: (a) E-plane boresight array pattern, as simulated (-) and measured (); (b) E-plane array pattern scanned to 40 degrees, as simulated (-) and measured (); (c) SLL versus scan angle based on the synthesized scan-specific phase tapers (—), with the phase taper optimized for boresight radiation (— —), with uniform taper (▪▪▪); (d) realized gain scan loss with the synthesized scan-specific phase tapers (—), with the phase taper optimized for boresight radiation (— —), with uniform taper (▪▪▪).

Table 2: Alternative methods for phased antenna array synthesis: a qualitative comparison.

Method	Handleable array sizes (elements)	Modeling fidelity	Comp. speed, realizability	Automation suitability as demonstrated*
IFT/IFFT	Very large (thousands)	AF	Very fast (FFT-based), yes	High
Matrix inversion	Medium (dozens)	AF	Moderate, yes	Low-to-medium
Gradient-based with smart search	Up to large (hundreds)	AF, Vectorial EM***	Moderate-to-fast**, yes	Medium-to-high
Deterministic AAP-based	Up to very large (thousands)	AF	Fast	Medium-to-high
Deterministic ADT-based	Up to very large (thousands)	AF	Fast yet with enumeration	Medium

*Suitability for automation within the phased array development process. ** Fast with analytical derivatives, and very fast for EM-level of description if enhanced by surrogate-based optimization. *** As well as circuit scattering signals (e.g., active reflection coefficients).

Table 3: The matrix inversion synthesis method: applications and features.

Array aperture	Pattern	Elements/size	Synthesis	Variables	Work
Linear	Symmetric sum, unsymmetric sum, two beams, monotonically decaying sidelobes	10, 18, 28, 38, 15	Chebyshev SLLs, −20 and −40 dB two side SLLs and alternating SLLs with uniform and nonuniform separation	Unconstrained amplitudes and phases	[41, 42]

Table 4: Gradient-based optimization synthesis: selected applications and features.

Array aperture	Pattern	Elements/size	Synthesis	Variables	Work
Linear	End-fire	10, 20, 40	AF-based SLL minimization AF-based SLL minimization with directivity maximization AF-based SLL minimization with nulling	Constrained element separations, amplitudes, and phases	[44, 45]

Table 4: Continued.

Array aperture	Pattern	Elements/size	Synthesis	Variables	Work
Linear	Sum, Sector beam		AF-based SLL minimization with nulling AF-based sector beam shaping with SLL minimization	Amplitudes and spacing; amplitudes, phases, and spacing	[44, 45]
Linear	Sum	32 symmetric	AF-based SLL minimization EM-based SLL minimization combined with active reflection control	Constrained nonuniform element separations, phases; constrained element spacing, phases	[51, 52]
Linear aperture with integrated corporate feed	Sum	12 symmetric	Corporate feed constrained synthesis for Chebyshev sidelobes EM-based SLL minimization*	Constrained power splits of the corporate feed junctions	[53]
Linear	Sum	16	Scan table using EM-based SLL minimization* at scanning	Phase tapers	[77]
Planar with square and skewed lattices	Sum	16 100	EM-based SLL minimization* combined with control of peak realized gain and active reflection coefficients EM-based SLL minimization* combined with control of active reflections	Constrained amplitudes and phases	[54]

*Within surrogate-based techniques for computational speed-up of pattern syntheses.

Table 5: AAP-based deterministic synthesis method: applications and features.

Array aperture	Pattern	Elements/size	Synthesis	Variables	Work
Linear sparse flat	Sum	24	Equally rippled reduced SLL	Constrained element separations	[56]
Sparse planar	Sum	1122	Reduced SLL	Constrained element separations and amplitudes (3-level control)	[56]
Linear sparse conformal	Symmetric sum Sector beam	28 30	Magnitude and phase pattern Isolux illumination	Constrained separations, amplitudes (4-level-control), and phases	[59]

Table 6: ADT-based deterministic synthesis method: applications and features.

Array aperture	Pattern	Elements/size	Synthesis	Variables	Work
Linear sparse	Sum	17, 37, 2000	Minimal SLL with unconstrained and constrained array length	Dilated element separations, unconstrained and constrained	[60]

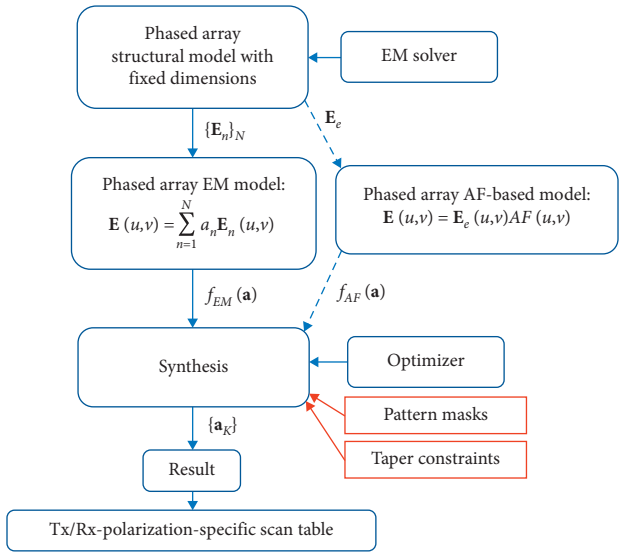

Figure 18: Simplified diagram of a phased antenna array pattern synthesis with nonidentical far-field responses of the embedded radiating elements.

computational cost of the synthesis procedure in the part relevant to the acquisition of the element-specific far-field distributions $\mathbf{E}_n$.

The polarization-specific EIRP patterns and peak values, with any complex taper applied to the radiating aperture, are readily available for evaluation and/or synthesis purposes at the EM level of description through any form of (4)–(7) with

$$\mathrm{EIRP}(\theta,\phi)_l\,[\mathrm{d}Bm] = p_{e,\max}\,[\mathrm{d}Bm] + 20\log_{10}\left|\mathbf{l}\cdot\mathbf{E}(\theta,\phi)_t\left[\frac{V}{m}\right]\right| - 14.77, \quad (9)$$

where $p_{e,\max}$ stands for the available power maximum at the BFIC TX outputs (depicted with the BFIC solder balls in Figure 15). The subscript t which denotes the total electric field indicates the evaluation with a complex taper normalized to its maximal amplitude, and the subscript l and unit vector $\mathbf{l}$ both refer to a particular polarization of the total far-field.

The insertion losses associated with transmission lines and transitions integrated in the array beamforming network are included in (9) if the ports in the EM-simulated model are defined at the BFIC TX outputs. In the case of uniform excitation, following a number of assumptions (including $\mathbf{E}_e = \mathbf{E}_n$ for all the radiators) and evaluating the element realized gain as

$$G_{e,\max}\,[\mathrm{d}B] + p_e\,[\mathrm{d}BW] = 20\log_{10}\left|\mathbf{E}_e\,(r = 1m)\right|_{\max} - 14.77. \quad (10)$$

Expression in (9) reduces to a well-known yet simplistic formula that is indispensable for quick system-level calculations (see (1) in [65] or (2) in [17] or [78]).

5. Conclusions

Based on a detailed analysis and comparison of methods, summarized in Table 2, and by considering the application scope and features of the considered approaches listed in Tables 1 and 3–6, it can be concluded that the IFT method suits the development of large linear and planar phased array apertures, with a sufficient AF description. The matrix inversion method is suitable for fast array prototyping because it relies on user decisions (or needs intelligent routines) to address the synthesis problem while tracking the locations of the sidelobe peaks at each iteration. The deterministic methods are inexpensive and versatile, and they are capable of synthesizing aperiodic (using AAP and ADT methods) and conformal (using AAP method) array grids. The AAP method accounts for the angular dependence of the element pattern; however, it does not account for nonidentical far-fields of the array elements. In the development of active phased arrays for 5G applications where EM-simulation-based description is necessary, the far-field synthesis through gradient-based optimization combined with a smart random search can be used. The need for EM simulation is dictated by the nonidentical far-fields of the embedded array elements, different polarization characteristics, or both (as a part of the process relevant to the pattern synthesis depicted in Figure 18). Furthermore, this method has a higher efficiency as compared to population-based optimizers. In addition, the surrogate-based methodology can significantly reduce the overall cost of EM-based syntheses during the acquisition of the vectorial far-field EM-based models of 5G active phased arrays.

Conflicts of Interest

The authors declare that they have no conflicts of interest.

References

[1] T. S. Rappaport, S. Sun, R. Mayzus et al., "Millimeter wave mobile communications for 5G cellular: it will work!" *IEEE Access*, vol. 1, pp. 335–349, 2013.

[2] E. Dahlman, S. Parkvall, J. Skold, and N. R. 5G, *The Next Generation Wireless Access Technology*, Academic Press, London, UK, 2018.

[3] W. Hong, Z. H. Jiang, C. Yu et al., "Multibeam antenna technologies for 5G wireless communications," *IEEE Transactions on Antennas and Propagation*, vol. 65, no. 12, pp. 6231–6249, 2017.

[4] S. Kutty and D. Sen, "Beamforming for millimeter wave communications: an inclusive survey," *IEEE Communications Surveys & Tutorials*, vol. 18, no. 2, pp. 949–973, 2016.

[5] A. B. Smolders, A. Dubok, N. M. Tessema et al., "Building 5G millimeter-wave wireless infrastructure: wide-scan focal-plane arrays with broadband optical beamforming," *IEEE Antennas and Propagation Magazine*, vol. 61, no. 2, pp. 53–62, 2019.

[6] R. L. Haupt and Y. Rahmat-Samii, "Antenna array developments: a perspective on the past, present and future," *IEEE Antennas and Propagation Magazine*, vol. 57, no. 1, pp. 86–96, 2015.

[7] T. C. Cheston and J. Frank, "Phased array radar antennas," in *Chapter 7 in Radar Handbook*, M. I. Skolnik, Ed., McGraw-Hill, Boston, MA, USA, 2nd edition, 1990.

[8] R. C. Hansen, *Phase Array Antennas*, Wiley, Hoboken, NJ, USA, 2nd edition, 2009.

[9] Dassault Systèmes, *CST Studio Suite 2020*, Dassault Systèmes, Meudon, France, 2020.

[10] Ansys Inc, *Ansys HFSS 2020 R1*, Ansys Inc, Canonsburg, PA, USA, 2020.

[11] COMSOL, Inc., *Multiphysics Ver. 5.4, 2020*, COMSOL, Inc., Burlington, MA, USA, 2020.

[12] Sonnet Software, Inc., *Sonnet Release 16*, Sonnet Software, Inc., Syracuce, NY, USA, 2018.

[13] S. Ghosh and D. Sen, "An inclusive survey on array antenna design for millimeter-wave communications," *IEEE Access*, vol. 7, pp. 83137–83161, 2019.

[14] D. Caratelli, A. Al-Rawi, J. Song, and D. Favreau, "Dielectric resonator antenna arrays for 5G wireless communications," *Microwave Journal*, pp. 36–46, 2020.

[15] S. Alkaraki and Y. Gao, "Mm-wave low-cost 3D printed MIMO antennas with beam switching capabilities for 5G communication systems," *IEEE Access*, vol. 8, pp. 32531–32541, 2020.

[16] G. Raney, B. Unruh, R. Lovestead, and B. Winther, "64-Element 28 gigahertz phased array 5G prototyping platform," in *Proceedings of 2018 11th Global Symposium on Millimeter Waves (GSMM)*, pp. 1–4, Boulder, CO, USA, May 2018.

[17] U. Kodak, B. Rupakula, S. Zihir, and G. M. Rebeiz, "60-GHz 64- and 256-element dual-polarized dual-beam wafer-scale phased-array transceivers with reticle-to-reticle stitching," *IEEE Transactions on Microwave Theory and Techniques*, vol. 68, no. 7, pp. 2745–2767, 2020.

[18] P. Hindle, "Comprehensive survey of commercial mmWave phased array companies. Focused on SATCOM and 5G applications," *Microwave Journal*, 2020.

[19] M. Jones and P. Delos, "Integrated transceivers simplify design, improve phased array radar performance," *Microwave Journal*, 2020.

[20] M. Alibakhshikenari, F. Babaeian, B. S. Virdee et al., "A comprehensive survey on "various decoupling mechanisms with focus on metamaterial and metasurface principles applicable to SAR and MIMO antenna systems"," *IEEE Access*, vol. 8, pp. 192965–193004, 2020.

[21] A. Iqbal, O. A. Saraereh, A. W. Ahmad, and S. Bashir, "Mutual coupling reduction using F-shaped stubs in UWB-mimo antenna," *IEEE Access*, vol. 6, pp. 2755–2759, 2018.

[22] C. W. Carroll and B. V. K. Vijaya Kumar, "Iterative Fourier transform phased array radar pattern synthesis," *Proceedings of SPIE*, vol. 827, pp. 73–84, 1987.

[23] J. R. Fienup, "Phase retrieval algorithms: a comparison," *Applied Optics*, vol. 21, no. 15, pp. 2758–2769, 1982.

[24] S. J. Stirland, "Fast antenna synthesis by an iterative FFT procedure," in *Proceedings of 1991 21st European Microwave Conference*, pp. 745–750, Stuttgart, Germany, September 1991.

[25] W. P. M. N. Keizer, "Fast low-sidelobe synthesis for large planar array antennas utilizing successive fast Fourier transforms of the array factor," *IEEE Transactions on Antennas and Propagation*, vol. 55, no. 3, pp. 715–722, 2007.

[26] W. P. M. N. Keizer, "Affine transformation for synthesis of low sidelobe patterns in planar array antennas with a triangular element grid using the IFT method," *IET Microwaves, Antennas & Propagation*, vol. 14, no. 8, pp. 830–834, 2020.

[27] W. P. M. N. Keizer, "Element failure correction for a large monopulse phased array antenna with active amplitude weighting," *IEEE Transactions on Antennas and Propagation*, vol. 55, no. 8, pp. 2211–2218, 2007.

[28] W. P. M. N. Keizer, "Linear array thinning using iterative FFT techniques," *IEEE Transactions on Antennas and Propagation*, vol. 56, no. 8, pp. 2757–2760, 2008.

[29] W. Keizer, "Large planar array thinning using iterative FFT techniques," *IEEE Transactions on Antennas and Propagation*, vol. 57, no. 10, pp. 3359–3362, 2009.

[30] W. P. M. N. Keizer, "Amplitude-only low sidelobe synthesis for large thinned circular array antennas," *IEEE Transactions on Antennas and Propagation*, vol. 60, no. 2, pp. 1157–1161, 2012.

[31] W. P. M. N. Keizer, "Low-sidelobe pattern synthesis using iterative fourier techniques coded in MATLAB [EM programmer's notebook]," *IEEE Antennas and Propagation Magazine*, vol. 51, no. 2, pp. 137–150, 2009.

[32] W. P. M. N. Keizer, "Synthesis of scan- and frequency-invariant low-sidelobe tapers for planar array antennas," *IEEE Transactions on Antennas and Propagation*, vol. 64, no. 8, pp. 3703–3707, 2016.

[33] W. P. M. N. Keizer, "Low sidelobe phased array pattern synthesis with compensation for errors due to quantized tapering," *IEEE Transactions on Antennas and Propagation*, vol. 59, no. 12, pp. 4520–4524, 2011.

[34] W. P. M. N. Keizer, "Planar phased-array antennas: mutual coupling and ultralow peak sidelobes," *IEEE Antennas and Propagation Magazine*, vol. 61, no. 1, pp. 14–28, 2019.

[35] W. P. M. N. Keizer, "Synthesis of monopulse antenna patterns for elliptical phased array antennas with different peak sidelobes along the principal planes," *IEEE Transactions on Antennas and Propagation*, vol. 67, no. 9, pp. 5943–5950, 2019.

[36] Y. Lo and S. Lee, "Affine transformation and its application to antenna arrays," *IEEE Transactions on Antennas and Propagation*, vol. 13, no. 6, pp. 890–896, 1965.

[37] M. Skolnik, J. Sherman, and F. Ogg Jr., "Statistically designed density-tapered arrays," *IEEE Transactions on Antennas and Propagation*, vol. 12, no. 4, pp. 408–417, 1964.

[38] W. P. M. N. Keizer, "APAS: an advanced phased-array simulator," *IEEE Antennas and Propagation Magazine*, vol. 52, no. 2, pp. 40–56, 2010.

[39] W. P. M. N. Keizer, "Synthesis of thinned planar circular and square arrays using density tapering," *IEEE Transactions on Antennas and Propagation*, vol. 62, no. 4, pp. 1555–1563, 2014.

[40] R. Willey, "Space tapaering of linear and planar arrays," *IRE Transactions on Antennas and Propagation*, vol. AP-10, no. 4, pp. 369–377, 1962.

[41] E. K. Miller, "Synthesizing linear-array patterns via matrix computation of element currents," *IEEE Antennas and Propagation Magazine*, vol. 55, no. 5, pp. 85–96, 2013.

[42] E. K. Miller, "Synthesis of scanning and nonuniformly spaced dolph-chebyshev arrays," in *Proceedings of 2016 IEEE/ACES International Conference on Wireless Information Technology and Systems (ICWITS) and Applied Computational Electromagnetics (ACES)*, pp. 1-2, Honolulu, HI, USA, March 2016.

[43] J. Mautz and R. Harrington, "Computational methods for antenna pattern synthesis," *IEEE Transactions on Antennas and Propagation*, vol. 23, no. 4, pp. 507–512, 1975.

[44] S. Koziel and S. Ogurtsov, "Design of linear antenna array apertures using surrogate-assisted optimization," in *Simulation-Based Optimization of Antenna Arrays*, pp. 213–251, World Scientific Publication, London, UK, 2019, Chapter 10.

[45] S. Koziel and S. Ogurtsov, "End-fire array synthesis using gradient-based numerical optimization with analytical derivatives," in *Proceedings of 2012 Loughborough Antennas & Propagation Conference (LAPC)*, pp. 1–4, Loughborough, UK, November 2012.

[46] S. Koziel and S. Ogurtsov, "Linear Antenna Array Synthesis Using Gradient-Based Optimization with Analytical Derivatives," in *Proceedings of the 2012 IEEE International Symposium on Antennas and Propagation*, pp. 1-2, Chicago, IL, USA, July 2012.

[47] C. A. Balanis, *Antenna Theory: Analysis and Design*, Wiley, Hoboken, NJ, USA, 4th edition, 2016.

[48] Math Works, Inc., *Optimization Toolbox User's Guide*, The MathWorks, Inc., Natick, MA, USA, 2020.

[49] W.-C. Weng, F. Yang, and A. Z. Elsherbeni, "Linear antenna array synthesis using taguchi's method: a novel optimization technique in electromagnetics," *IEEE Transactions on Antennas and Propagation*, vol. 55, no. 3, pp. 723–730, 2007.

[50] D. Gies and Y. Rahmat-Samii, "Particle swarm optimization for reconfigurable phase-differentiated array design," *Microwave and Optical Technology Letters*, vol. 38, no. 3, pp. 168–175, 2003.

[51] S. Koziel and S. Ogurtsov, "Phase-spacing optimization of linear microstrip antenna arrays by em-based superposition models," in *Proceedings of 2014 Loughborough Antennas and Propagation Conference (LAPC)*, pp. 26–30, Loughborough, UK, November 2014.

[52] S. Koziel and S. Ogurtsov, "Phase-spacing optimization of linear microstrip antenna arrays using simulation-based surrogate superposition models," *International Journal of RF and Microwave Computer-Aided Engineering*, vol. 25, no. 6, pp. 536–547, 2015.

[53] S. Koziel and S. Ogurtsov, "Design of low-sidelobe arrays implementing required excitation tapers: the case of corporate

feeds comprising unequal-split junctions," in *Simulation-Based Optimization of Antenna Arrays*, pp. 328–354, World Scientific Publ., London, UK, 2019, Section 14.2.

[54] S. Koziel and S. Ogurtsov, "Fast simulation-driven optimization of planar microstrip antenna arrays using surrogate superposition models," *International Journal of RF and Microwave Computer-Aided Engineering*, vol. 25, no. 5, pp. 371–381, 2015.

[55] D. Caratelli and M. C. Viganó, "Analytical synthesis technique for linear uniform-amplitude sparse arrays," *Radio Science*, vol. 46, no. 4, pp. 1–6, 2011.

[56] D. Caratelli and M. C. Vigano, "A novel deterministic synthesis technique for constrained sparse array design problems," *IEEE Transactions on Antennas and Propagation*, vol. 59, no. 11, pp. 4085–4093, 2011.

[57] D. Caratelli, M. C. Viganó, G. Toso, P. Angeletti, A. A. Shibelgut, and R. Cicchetti, "A hybrid deterministic/metaheuristic synthesis technique for non-uniformly spaced linear printed antenna arrays," *Progress In Electromagnetics Research*, vol. 142, pp. 107–121, 2013.

[58] D. Caratelli, G. Toso, O. V. Stukach, and N. V. Panokin, "Deterministic constrained synthesis technique for conformal aperiodic linear antenna arrays-Part I: theory," *IEEE Transactions on Antennas and Propagation*, vol. 67, no. 9, pp. 5951–5961, 2019.

[59] D. Caratelli, G. Toso, O. V. Stukach, and N. V. Panokin, "Deterministic constrained synthesis technique for conformal aperiodic linear antenna arrays-Part II: applications," *IEEE Transactions on Antennas and Propagation*, vol. 67, no. 9, pp. 5962–5973, 2019.

[60] A. Kedar, "Deterministic synthesis approach for linear sparse array antennas," *IEEE Transactions on Antennas and Propagation*, vol. 68, no. 9, pp. 6667–6674, 2020.

[61] J. W. Hooker and R. K. Arora, "Optimal thinning levels in linear arrays," *IEEE Antennas and Wireless Propagation Letters*, vol. 9, pp. 771–774, 2010.

[62] A. Kedar and L. P. Ligthart, "Wide scanning characteristics of sparse phased array antennas using an analytical expression for directivity," *IEEE Transactions on Antennas and Propagation*, vol. 67, no. 2, pp. 905–914, 2019.

[63] S. Zhang, X. Chen, I. Syrytsin, and G. F. Pedersen, "A planar switchable 3-D-coverage phased array antenna and its user effects for 28-GHz mobile terminal applications," *IEEE Transactions on Antennas and Propagation*, vol. 65, no. 12, pp. 6413–6421, 2017.

[64] X. Chen, M. Abdullah, S. Zhang, T. Li, and Q. Li, "Mutual coupling reduction of slot array antenna for 5G millimeter-wave handset," in *Proceedings of 2019 Photonics & Electromagnetics Research Symposium-Fall (PIERS-Fall)*, pp. 1525–1530, Xiamen, China, December 2019.

[65] K. Kibaroglu, M. Sayginer, and G. M. Rebeiz, "A low-cost scalable 32-element 28-GHz phased array transceiver for 5G communication links based on a 2×2 beamformer flip-chip unit cell," *IEEE Journal of Solid-State Circuits*, vol. 53, no. 5, pp. 1260–1274, 2018.

[66] K. Kibaroglu, M. Sayginer, T. Phelps, and G. M. Rebeiz, "A 64-element 28-GHz phased-array transceiver with 52-dBm EIRP and 8-12-Gb/s 5G link at 300 meters without any calibration," *IEEE Transactions on Microwave Theory and Techniques*, vol. 66, no. 12, pp. 5796–5811, 2018.

[67] A. Nafe, M. Sayginer, K. Kibaroglu, and G. M. Rebeiz, "2 $\times$ 64-element dual-polarized dual-beam single-aperture 28-GHz phased array with 2 $\times$ 30 Gb/s links for 5G polarization MIMO," *IEEE Transactions on Microwave Theory and Techniques*, vol. 68, no. 9, pp. 3872–3884, 2020.

[68] M. K. Leino, R. Montoya Moreno, J. Ala-Laurinaho, R. Valkonen, and V. Viikari, "Waveguide-based phased array with integrated element-specific electronics for 28 GHz," *IEEE Access*, vol. 7, pp. 90045–90054, 2019.

[69] B. Rupakula, S. Zihir, and G. M. Rebeiz, "Low complexity 54-63-GHz transmit/receive 64- and 128-element 2-D-scanning phased-arrays on multilayer organic substrates with 64-QAM 30-gbps data rates," *IEEE Transactions on Microwave Theory and Techniques*, vol. 67, no. 12, pp. 5268–5281, 2019.

[70] M. K. Leino, J. Bergman, J. Ala-Laurinaho, and V. Viikari, "Beam optimization for 28 GHz phased array utilizing measurement data," in *Proceedings of 2020 14th European Conference on Antennas and Propagation (EuCAP)*, pp. 1–5, Copenhagen, Denmark, March 2020.

[71] Y. Yin, S. Zihir, T. Kanar et al., "A 37-42-GHz 8×8 phased-array with 48-51-dBm EIRP, 64-QAM 30-Gb/s data rates, and EVM analysis versus channel RMS errors," *IEEE Transactions on Microwave Theory and Techniques*, vol. 68, no. 11, pp. 4753–4764, 2020.

[72] A. H. Aljuhani, T. Kanar, S. Zihir, and G. M. Rebeiz, "A scalable dual-polarized 256-element Ku-band SATCOM phased-array transmitter with 36.5 dBW EIRP per polarization," in *Proceedings of 2018 48th European Microwave Conference (EuMC)*, pp. 938–941, Madrid, Spain, September 2018.

[73] X. Gu, D. Liu, C. Baks et al., "Development, implementation, and characterization of a 64-element dual-polarized phased-array antenna module for 28-GHz high-speed data communications," *IEEE Transactions on Microwave Theory and Techniques*, vol. 67, no. 7, pp. 2975–2984, 2019.

[74] G. Gültepe, S. Zihir, T. Kanar, and G. M. Rebeiz, "A dual-polarized 1024-element Ku-band SATCOM transmit phased-array with ±70° scan and 43.5 dBW EIRP," in *Proceedings of 2020 IEEE/MTT-S International Microwave Symposium (IMS)*, pp. 837–840, Los Angeles, CA, USA, August 2020.

[75] K. Park, J. Myeong, G. M. Rebeiz, and B.-W. Min, "A 28-GHz full-duplex phased array front-end using two cross-polarized arrays and a canceller," *IEEE Transactions on Microwave Theory and Techniques*, vol. 69, no. 1, pp. 1127–1135, 2021.

[76] Y. Yin, B. Ustundag, K. Kibaroglu, M. Sayginer, and G. M. Rebeiz, "Wideband 23.5-29.5-GHz phased arrays for multistandard 5G applications and carrier aggregation," *IEEE Transactions on Microwave Theory and Techniques*, vol. 69, no. 1, pp. 235–247, 2021.

[77] S. Koziel and S. Ogurtsov, "Design of linear phased array apertures using response correction and surrogate-assisted optimization," in *Simulation-Based Optimization of Antenna Arrays*, pp. 357–371, World Scientific Publication, London, UK, 2019, Chapter 15.

[78] B. Peterson and D. Schnaufer, "5G fixed wireless access array and RF-front end trade-offs," *Microwave Journal*, 2018.